Proceedings of ASME Turbo Expo 2011
GT2011
June 6-10, 2011, Vancouver, British Columbia, Canada

GT2011-45338

ROTOR-TIP FLOW FIELDS NEAR INCEPTION POINT OF ROTATING INSTABILITY IN AN AXIAL-FLOW FAN

Takahiro Nishioka, Toshio Kanno
Hitachi Plant Tecnologies, Ltd.
603, Kandatsu, Tsuchiura, Ibaraki, 300-0013 Japan

Kiyotaka Hiradate
Hitachi, Ltd.
832-2, Horiguchi, Hitachinaka, Ibaraki, 312-0034 Japan

ABSTRACT

Stall inception patterns at three stagger-angle settings for the highly loaded rotor blades were experimentally investigated in a low-speed axial-flow fan. Rotor-tip flow fields were also numerically investigated to clarify the mechanism behind the stall inception from a rotating instability. The rotating instability is confirmed near stall condition at the high stagger-angle settings for the highly loaded rotor blades as same as that for the moderate loaded rotor blades. The rotating instability is induced by an interaction between the incoming flow, the reversed tip-leakage flow, and the end-wall backflow from the trailing edge. At the high stagger-angle settings for the rotor blades, the interface between the incoming flow and the reversed tip leakage flow becomes parallel to the leading edge plane near and at the stall condition. Moreover, the tip leakage flow spills from the leading edge of the adjacent blade at the stall condition. The changes in the end-wall flow at the rotor tip are consistent with the criteria for the spike initiation suggested by Vo et al. and Hah et al. However, the short length-scale stall cell is not observed at the high stagger-angle settings. The tip-leakage vortex breakdown is confirmed at the three stagger-angle settings. The end-wall blockage induced by the tip-leakage vortex breakdown influences the development of the stall cell. Moreover, the development of the three-dimensional separation vortex induced by the tip-leakage vortex breakdown seems to be one of the criteria for spike-type stall inception.

INTRODUCTION

Rotating stall is an aerodynamic instability that limits the stable operating range of axial-flow compressors and fans. Extensive studies have been carried out to clarify the mechanism responsible for stall inception. It is well known that there are two distinctive routes to rotating stall in compressors and fans. The first inception pattern begins with a short length-scale stall cell. This pattern is known as “spike stall inception”. Day [1], Camp and Day [2], and Inoue et al. [3] investigated the features of spike stall inception. The second pattern begins with a long length-scale disturbance, which appears prior to the formation of a fully developed stall cell. This pattern is known as “modal stall inception”. Garnier et al. [4] confirmed that the modal oscillation was a small-amplitude wave that propagated at a speed slightly less than the fully developed stall-cell speed. Stall inception, which contains both spike and modal disturbance was observed by Day [1].

Another short length-scale disturbance, which does not lead directly to stall, has also been observed in low-speed compressors. This disturbance is called “rotating instability”. Mailach [5] and Mailach et al. [6] observed the rotating instability in a narrow operating range near the stability limit when the tip clearances were relatively large. März et al. [7, 8] also observed rotating instability near the operating limit at the large stagger-angle setting for the rotor blades with relatively large tip clearance. Moreover, März et al. [8] found that the rotating instability was induced by the interaction between the incoming flow, the reversed tip-leakage flow, and the end wall backflow from the trailing edge of the rotor blade.

Our previous studies [9, 10], which used moderate loaded rotor blades with the hub to tip ratio of 0.57, clarified that stall inception depended on the stagger-angle settings for the rotor blades. The spike stall inception was observed at the design stagger-angle setting, and the modal stall inception was observed at the small stagger-angle setting [9]. Stall inception from the rotating instability was also observed at the large

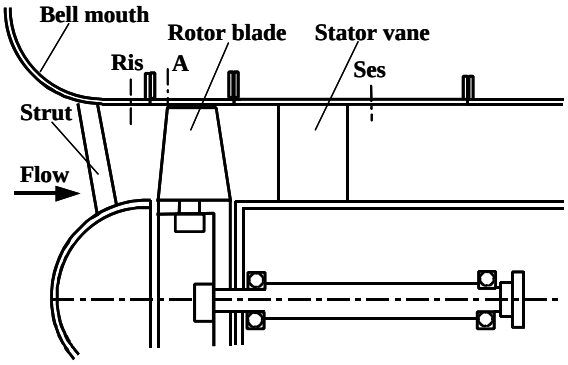

Fig. 1 Schematic diagram of fan

Table 1 Design specifications of fan

Tip diameter	**628mm**
Hub/tip ratio	**0.62**
Rotation tip speed	**99 m/s**
Number of rotor blades	**16**
Number of stator vanes	**21**
Rotor tip clearance (% of rotor tip chord)	**2.0%**

Table 2 Design specifications of rotor and stator

		Rotor		
	R / R_t	**Solidity**	**Stagger-angle (deg.)**	**Maximum thickness**
Tip	**1.00**	**0.60**	**60.6**	**6.0%**
Mid	**0.83**	**0.80**	**52.4**	**7.8%**
Hub	**0.62**	**1.21**	**33.0**	**10.0%**
		Stator		
Tip	**1.00**	**1.06**	**11.4**	**10.0%**
Mid	**0.83**	**1.27**	**12.6**	**10.0%**
Hub	**0.62**	**1.70**	**13.9**	**10.0%**

stagger-angle setting [10]. Moreover, the influence of the end wall flow at the rotor tip on the stall inception was experimentally and numerically investigated [11, 12,13].

In the current paper, the stall inception patterns at three stagger-angle settings for the highly loaded rotor blades, which hub to tip ratio was 0.62, were experimentally investigated. Moreover, the end wall flow fields at the rotor tip were numerically investigated to elucidate the mechanism of rotating stall inception from the rotating instability.

NOMENCLATURE

Cp' = Pressure fluctuation coefficient based on rotor tip speed
F= Rotor rotation frequency
f= frequency
Hn=Normalized helicity
PFL=Pressure fluctuation level based on rotor tip speed
T= Rotor rotation period
t= Time
U=Rotor rotation speed
W=Relative velocity
ϕ= Flow-rate coefficient based on rotor tip speed
ψ= Pressure-rise coefficient based on rotor tip speed

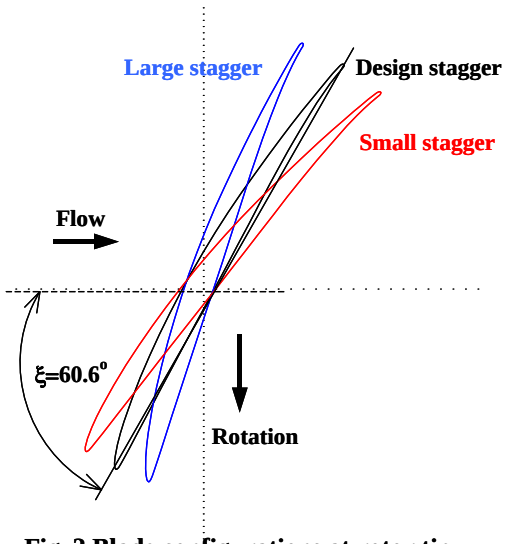

Fig. 2 Blade configurations at rotor tip

ξ= Rotor stagger angle
Subscripts
t=Rotor tip

EXPERIMENTAL STUDY

Facility and measurement method

A schematic diagram of the low-speed axial-flow fan is shown in Fig. 1, and its design specifications are listed in Table 1. The design flow-rate coefficient is 0.44, and the total-to-total pressure-rise coefficient is 0.43. The tip clearance for the rotor blades is 2.0% of the rotor tip chord-length. The rotor blades were designed for the free vortex operation under the axial inlet-flow condition. The stator vanes were designed for the constant exit-flow angle. The design specifications for the rotor blade and the stator vane are listed in Table 2.

The stall-inception pattern was investigated at three stagger-angle settings for the rotor blades. One was the design stagger-angle setting. The others were the large and the small stagger-angle settings that were 10 degrees larger and smaller than the design value, respectively. The configurations of the rotor blade at the tip are shown in Fig. 2.

The fan performance was evaluated in terms of the inlet-total to exit-total pressure rise. The inlet-total pressure was obtained by summing the measured wall static pressure and the dynamic pressure calculated from the flow rate. The measurement points for the static pressure at the inlet and the outlet of the fan are shown as Ris and Ses in Fig. 1, respectively. The flow rate was measured using a flow nozzle located upstream of the bell mouth.

Pressure fluctuation on the casing wall was measured using a high-response pressure transducer (Kulite XT-140). The transducer was mounted on the casing wall at the rotor leading edge (A in Fig. 1). All measurements were performed under the fixed-throttle conditions. A low-pass filter was applied to the instantaneous pressure fluctuation to remove the blade passing frequency (BPF) component. The stall-inception pattern was estimated by the filtered instantaneous pressure-fluctuation and the averaged spectrum of pressure fluctuation at A. The averaged spectra were obtained with a FFT analyzer.

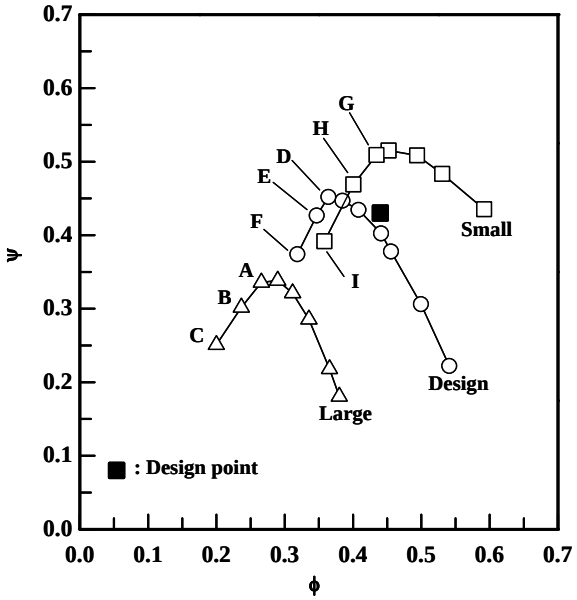

Fig. 3 Pressure-rise characteristics at three stagger-angle settings for rotor blades

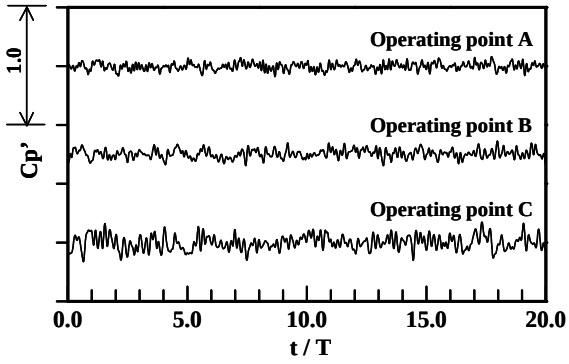

Fig. 4 Pressure fluctuation near and at stall condition at large stagger-angle setting

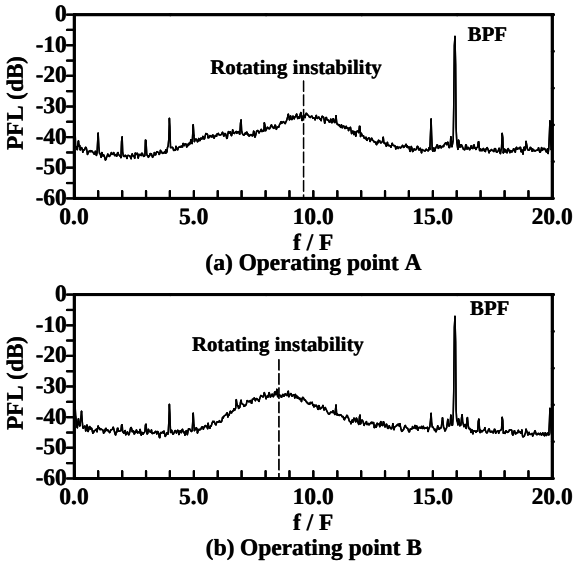

Fig. 5 Pressure fluctuation spectra near stall condition at large stagger-angle setting

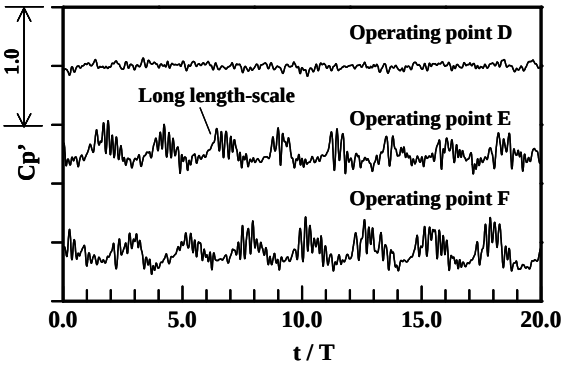

Fig. 6 Pressure fluctuation near and at stall condition at design stagger-angle setting

Pressure-rise characteristics and stall inception patterns

Figure 3 plots the pressure-rise characteristics of the fan. In this paper, the flow-rate coefficients (ϕ) of 0.266, 0.236, and 0.200 at the large stagger-angle setting for the rotor blades are designated as operating points A, B, and C, respectively, and the flow-rate coefficients of 0.364, 0.347, and 0.319 at the design stagger-angle are designated as operating points D, E, and F, respectively. Moreover, the flow-rate coefficients of 0.434, 0.401, and 0.358 at the small stagger-angle setting are designated as operating points G, H, and I, respectively.

Figure 4 shows instantaneous pressure fluctuations near and at the stall condition. The abscissa indicates non-dimensional time (t/T) divided by the period of the rotor rotation, and the ordinate indicates pressure fluctuation coefficient (Cp') divided by the rotor tip speed, respectively. A precursor indicating a stall cell is not observed through operating points A to C.

Figure 5 shows pressure fluctuation spectra at the large stagger-angle setting. The abscissa indicates non-dimensional frequency (f/F) divided by the rotor rotation frequency, and the ordinate indicates pressure fluctuation level (PFL) divided by the rotor tip speed, respectively. A hump of the pressure fluctuation is observed at operating points A and B, although the fluctuation indicating the stall cell is not observed in the instantaneous pressure fluctuation. The center frequency of hump shifts from f/F=9.5 to f/F=8.5, which is about one-half of the blade passing frequency (BPF), as operating point moves A to B.

Figure 6 shows instantaneous pressure fluctuations near and at the stall condition at the design stagger-angle. The fluctuation indicating a long length-scale stall cell is observed at operating points E and F. The hump is also observed at operating point D in the pressure fluctuation spectrum shown in Fig. 7 (a). The center frequency of the hump shifts from f/F=10.0 to f/F=9.0 as operating point moves D to E. The peak indicating the long length-scale stall cell is also observed at operating point E.

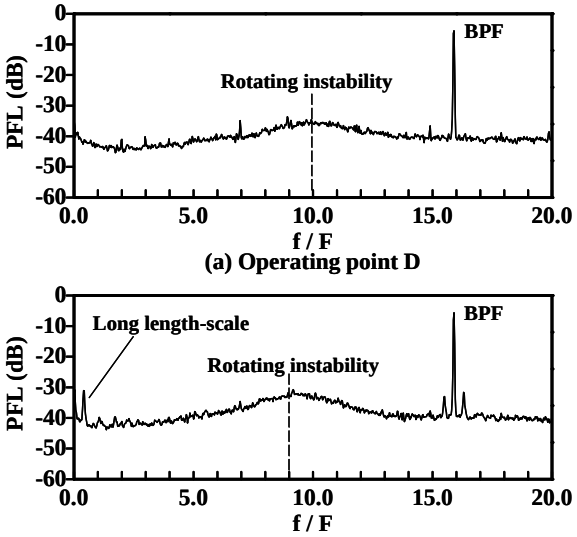

Fig. 7 Pressure fluctuation spectra near stall condition at design stagger-angle setting

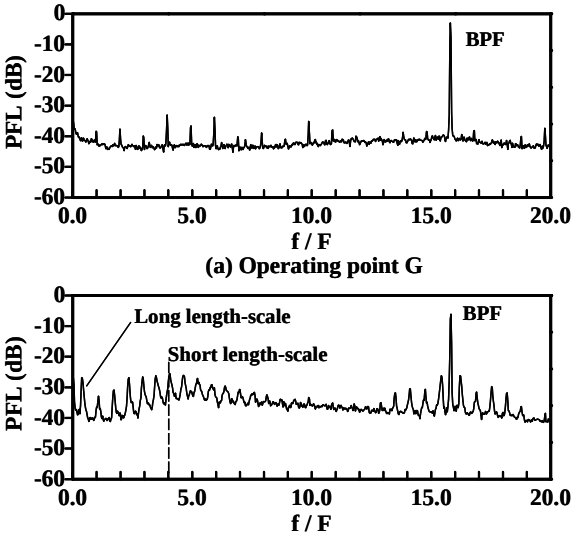

Fig. 9 Pressure fluctuation spectra near stall condition at small stagger-angle setting

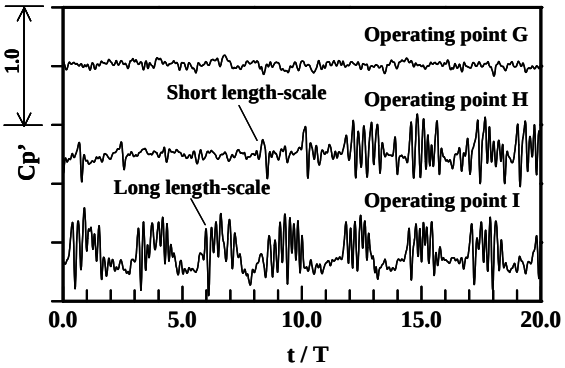

Fig. 8 Pressure fluctuation near and at stall condition at small stagger-angle setting

März et al [8] confirmed the rotating instability indicated by the hump at roughly one-half of the BPF. A similar hump is observed near the peak pressure-rise point at the large and design stagger-angle settings shown in Figs. 5 and 7. It is confirmed from the experimental results that the rotating instability occurs at the large and design stagger-angle settings. However, the stall cell does not develop at the large stagger-angle setting, and the long length-scale stall cell develops after the rotating instability occurs at the design stagger-angle setting.

Figure 8 shows the instantaneous pressure fluctuation at the small stagger-angle setting. A short length-scale stall cell first appears, and then the long length-scale stall cell develops at operating point H. The long length-scale stall cell is periodically observed at operating point I. The hump indicating the rotating instability is not observed at operating points G and H shown in Fig. 9. However, the peaks corresponding to the short length-scale stall cell are observed around f/F=4.0, and the peak corresponding to the long length-scale stall cell is also observed at f/F=0.3 at operating point H. It is confirmed from these results that the stall inception pattern at the small stagger-angle setting is a spike-type.

It is found from the experimental results at the three stagger-angle settings for the highly loaded rotor blades that the stall inception pattern depends on the rotor stagger-angle setting as same as that observed in the moderate loaded rotor blades [9, 10]. It is also found that the rotating instability occurs at the high stagger-angle setting for the rotor blades. The change in the stall inception patterns is considered to be influenced by the end-wall flow at the rotor-tip. Therefore, the detailed flow fields at the rotor tip are numerically investigated in the next section.

NUMERICAL STUDY

Numerical method

Figure 10 shows the computational model for this study. The influence of flow in the stator passage on the stall inception was considered to be smaller than that in the rotor passage, because the distance from the rotor trailing edge to the stator leading edge at the tip was 1.1 times of the rotor-tip chord length. Therefore, only the rotor blade passage was modeled for the calculations. Moreover, the eight blade passages in the rotor shown in Fig. 10 were modeled as the computational domain because the model of the eight blade passages yielded a better prediction for the stall inception point than that of the single passage model. The inlet boundary was placed upstream from the rotor leading edge by one hub chord length, and the outlet boundary was placed downstream from the trailing edge also by one hub chord length. The computational grid was generated using the ANSYS® TurboGrid™ 11.0 (ANSYS® TurboGrid™ 11.0 is registered trademark of ANSYS, inc.) . The grid in the tip clearance consisted of 40 nodes in the span-wise direction and 20 nodes on the tip. The grid in one blade

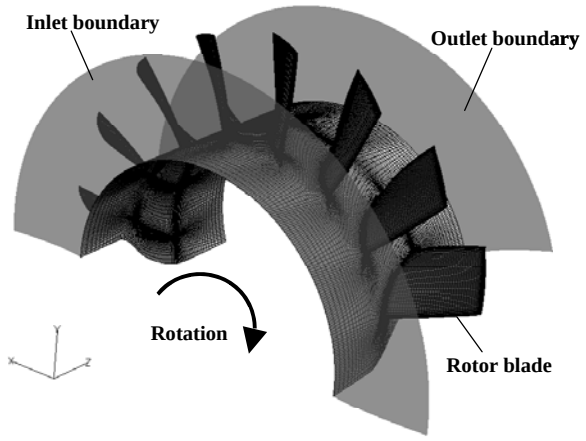

Fig. 10 Computational grid for rotor blades

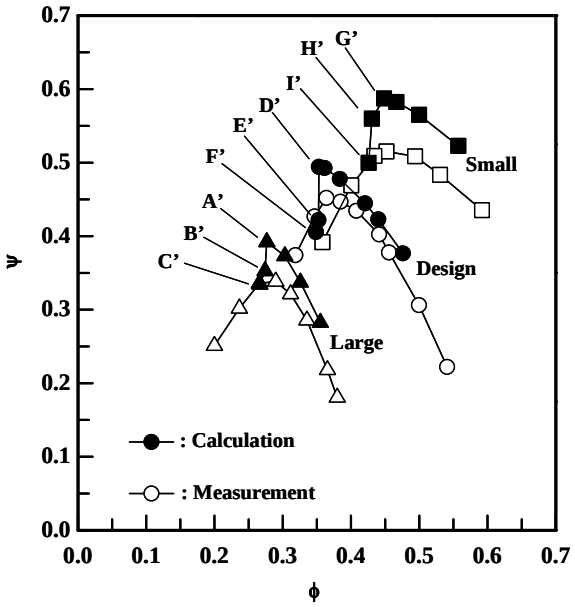

Fig. 11 Comparison of pressure-rise characteristics between calculation and measurement

passage contained about 565,224 nodes, and the whole grid contained 4,521,792 nodes. The y^+ on the blade surface was controlled below 5.

Three-dimensional compressible steady simulations were carried out using the commercial code ANSYS® CFX™ 11.0 (ANSYS® CFX™ 11.0 is registered trademark of ANSYS, inc.). A Share-stress transport (SST) model was applied as a turbulent model. The total pressure, total temperature, and flow angle were specified at the inlet boundary, and the mass flow rate was specified at the outlet boundary. Averaged total pressure-rise between the inlet and the outlet boundaries was compared with the measured total pressure-rise of the fan.

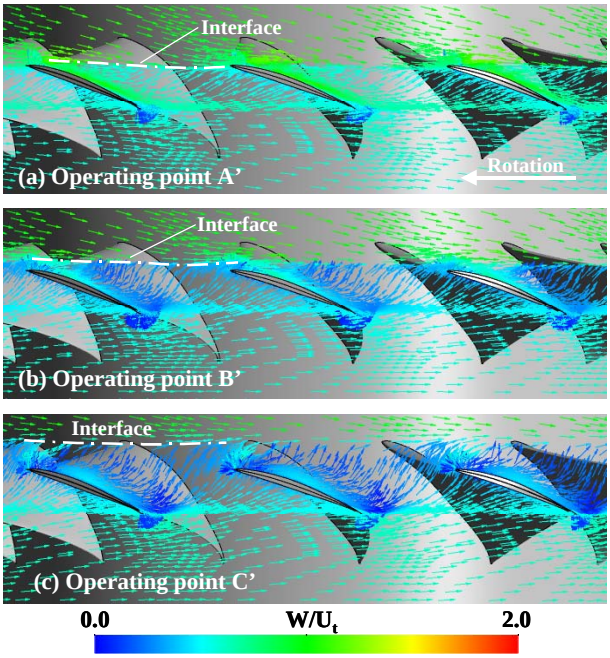

Fig. 12 Relative flow vector at rotor tip at large stagger-angle setting

Calculated pressure-rise in isolated rotor

Comparison of total pressure-rise characteristics between the calculation and the measurement is shown in Fig. 11. In the following section, the flow-rate coefficients of 0.277, 0.274, and 0.266 at the large stagger-angle setting used in the calculation are designated as operating points A', B', and C', respectively. The flow rate coefficients of 0.353, 0.352, and 0.349 at the design stagger-angle setting used in the calculation are designated as operating points D', E', and F', respectively. Moreover, the flow rate coefficients of 0.448, 0.431, and 0.426 at the small stagger-angle setting used in the calculation are designated as operating points G', H', and I', respectively.

The calculated characteristic at each stagger-angle setting is larger than the measured one, because the calculation result does not include the losses at the stator vanes (as shown in Fig.1). However, the flow rates at the maximum pressure-rise points in the calculations are almost the same as those in the measurements. Moreover, the change in calculated pressure-rise characteristic at each stagger-angle setting is similar to the measured characteristic. It is considered from the comparison of the pressure-rise characteristic that the flow fields in the rotor passage near and at the stall condition are simulated by the present calculations.

Behavior of end wall flow at rotor tip

Figure 12 shows relative flow vector at the 98% height from the rotor hub at the large stagger-angle setting. Backflow from the trailing edge initiates, and the tip leakage flow axially reverses at operating point A'. Moreover, the backflow develops, and the tip leakage flow spills from the leading edge of the adjacent blade at operating pints B' and C'. At the design stagger-angle setting shown in Fig. 13, the backflow from the trailing edge also initiates, and the tip leakage flow reverses at

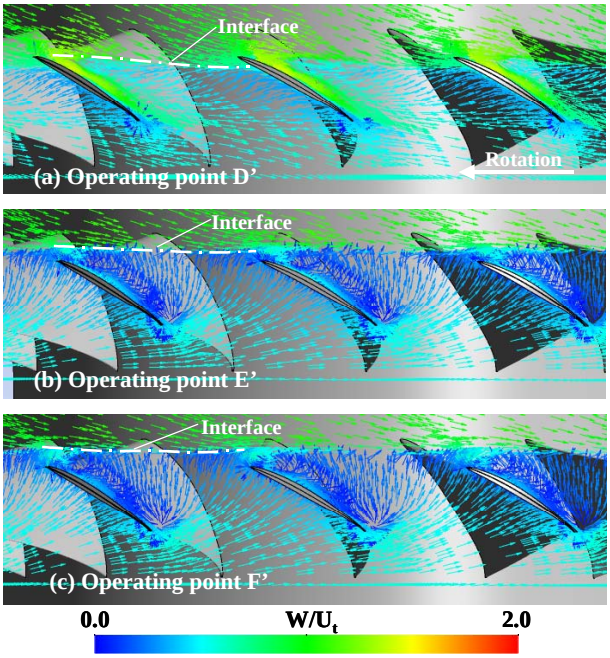

Fig. 13 Relative flow vector at rotor tip at design stagger-angle setting

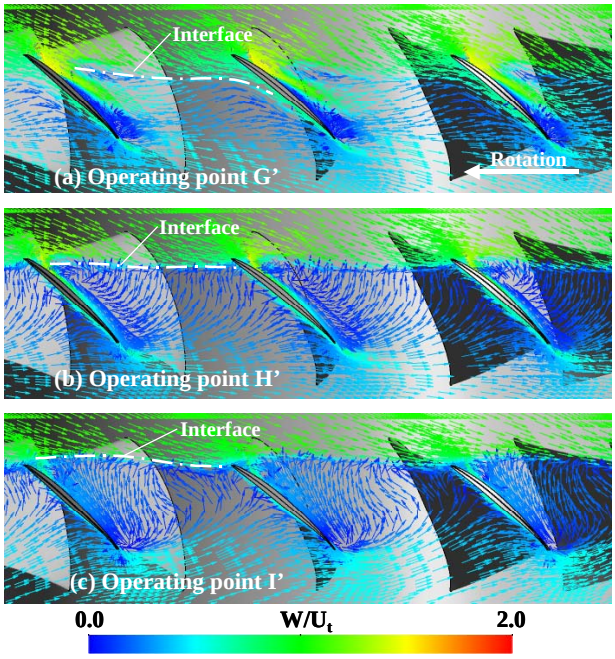

Fig. 14 Relative flow vector at rotor tip at small stagger-angle setting

operating points E'. Moreover, the tip leakage flow spills from the leading edge at operating pints E' and F'.

The rotating instability was experimentally confirmed near and at the stall condition at both large and design stagger-angle settings shown in Figs. 5 and 7. März et al. [8] found that the rotating instability was induced by an interaction between the incoming flow, the reversed tip-leakage flow, and the end-wall backflow from the trailing edge of the rotor blade. Similar interaction between the incoming flow, the reversed tip-leakage flow, and the end-wall backflow from the trailing edge is numerically confirmed at both large and design stagger-angle settings shown in Figs 12 and 13. It is also found from our experimental and numerical results that the rotating instability is induced by the interaction between the incoming flow, the reversed tip-leakage flow, and the end-wall backflow from the trailing edge.

Figure 14 shows relative flow vector at the rotor tip at the small stagger-angle setting. The backflow from the trailing edge initiates at operating point G'. The interface between the incoming flow and the reversed tip-leakage flow becomes parallel to the leading edge plane at operating points H' and I'. Moreover, the tip-leakage flow slightly spills from the leading edge of the adjacent blade at operating point I'.

Vo et al. [14] suggested two criteria necessary for the spike-type stall-inception. The first is the initiation of the backflow from the trailing edge. The second is that the interface between the tip leakage flow and the incoming flow becomes parallel to the leading edge plane. Vo et al. [14] and Hah et al. [15] also suggested that the forward spillage of the tip leakage flow develops at the leading edge in the spike-type stall condition.

The short length-scale stall cell is confirmed at the small stagger-angle setting shown in Fig. 8. The backflow from the trailing edge was numerically observed at operating point G'. Moreover, the interface between the incoming flow and the reversed tip-leakage flow becomes parallel to the leading edge plane at operating points H' and I', and the reversed tip-leakage flow slightly spills from the leading edge at operating point I'. The behaviors of the end-wall flow at the small stagger-angle settings are consistent with the criteria for the spike initiation suggested by Vo et al. [14] and Hah et al. [15].

At the large and design stagger-angle settings, the backflow from the trailing edge is observed, and the interface between the incoming flow and the reversed tip leakage flow becomes parallel to the leading edge plane shown in Figs. 12 and 13. Moreover, the tip leakage flow spills from the leading edge. The behaviors of end-wall flow at the large and design stagger-angle settings are also consistent with the criteria for the spike initiation suggested by Vo et al. [14] and Hah et al. [15]. However, the short length-scale stall cell is not observed. It is considered that another criterion is needed for the development of the short length-scale stall cell in the spike-type stall inception.

Behavior of tip leakage vortex

Figure 15 shows the behaviors of a tip leakage vortex at the large stagger-angle setting for the rotor blades. The tip leakage vortex is identified by a vortex core and tip leakage streamlines from the rotor leading edge. The vortex core is colored by normalized helicity [16]. The tip-leakage vortex extends to the pressure side of the adjacent blade at operating points A' and B', and reaches the leading edge at operating point C'. The tip leakage streamlines tightly spirals along the vortex core at operating point A' and expands in the blade passage as operating points moves B' to C'. The sign of the normalized helicity on the vortex core changes from negative to positive where the tip leakage streamlines expand.

At the design stagger-angle setting shown in Fig. 16, the tip-leakage vortex extends to the rotor exit through operating

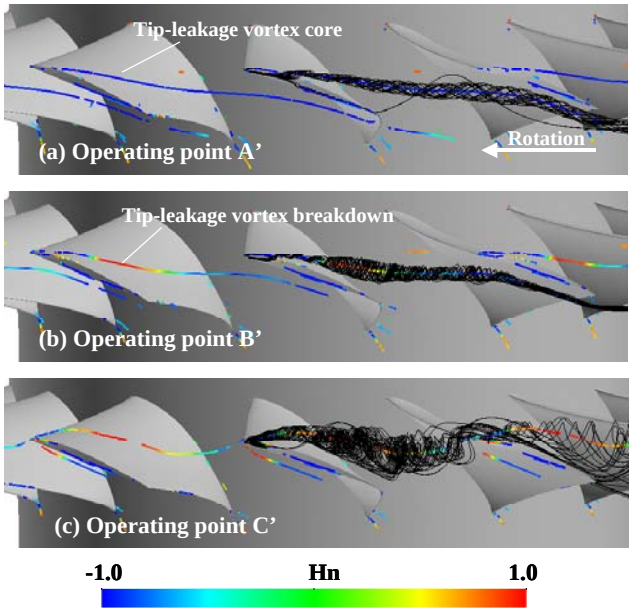

Fig. 15 Change in tip-leakage vortex at large stagger-angle setting

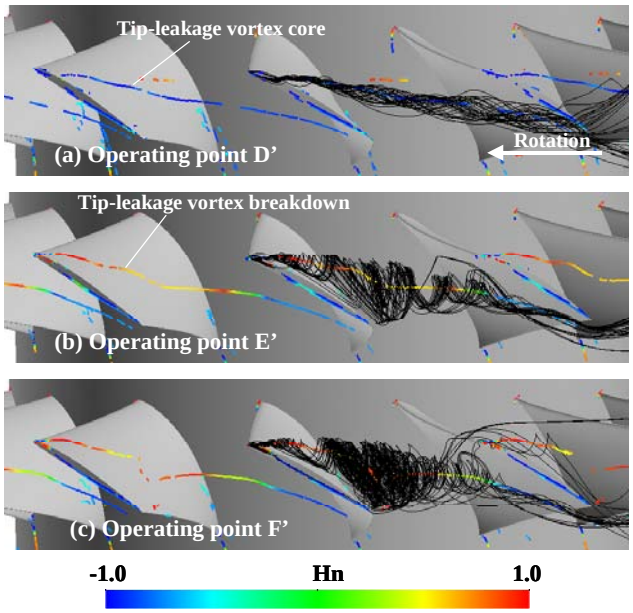

Fig. 16 Change in tip-leakage vortex at design stagger-angle setting

points D' to F', and the tip leakage streamlines largely expand at operating points E' and F'. The sign of the normalized helicity on the vortex core changes from negative to positive in the blade passage. Moreover, at the small stagger-angle setting shown in Fig. 17, the tip-leakage vortex also extends to the rotor exit at operating point G'. Another vortex core is observed near the rotor exit. The tip leakage streamlines spirals along the vortex core at operating point G' and expands in the blade passage at operating point H'. These streamlines do not roll up at operating point I'. The sign of the normalized helicity

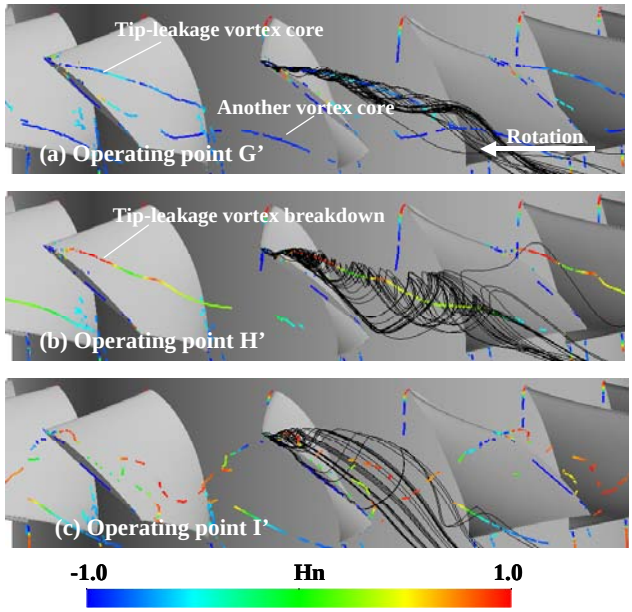

Fig. 17 Change in tip-leakage vortex at small stagger-angle setting

changes from negative to positive near the leading edge atoperating point H'.

Furukawa et al. [16, 17] suggested that the tip-leakage streamlines expand and the sign of the normalized helicity changes when the tip-leakage vortex breakdown occurs. It is confirmed by referring the study of Furukawa et al. [16, 17] that the tip-leakage vortex breakdown occurs at three stagger-angle settings for the rotor blades.

As mentioned in the experimental study, the stall cell does not develop at the large stagger-angle setting. In contrast, the long length-scale stall cell develops at the design stagger-angle setting, and the short length-scale stall cell develops at the small stagger-angle setting. As shown in Figs. 15, 16, and 17, the end-wall blockage induced by the tip-leakage vortex breakdown at the large stagger-angle setting is smaller than those blockages at the design and the small settings. It is considered that the end-wall blockage induced by the tip-leakage vortex breakdown influences the development of the stall cell.

Behavior of separated flow on blade suction surface

Figure 18 shows the limiting streamlines on the suction surface of the rotor blade and the tip-leakage vortex core at the large stagger-angle setting for the rotor blades. The limiting streamlines indicating outward secondary flow is observed near the hub through operating points A' to C'. The envelope of the limiting streamlines with convergence is observed near the leading edge at the rotor tip at operating points B' and C'. It is found that the leading edge separation occurs at operating points B' and C'.

At the design stagger-angle setting shown in Fig. 19, the outward secondary flow is observed near the hub through operating points D' to F'. The envelope of the limiting streamlines with convergence is observed at the rotor tip at operating points E' and F'. The outwards secondary flow near the hub is slightly suppressed at operating points E' and F'. It is

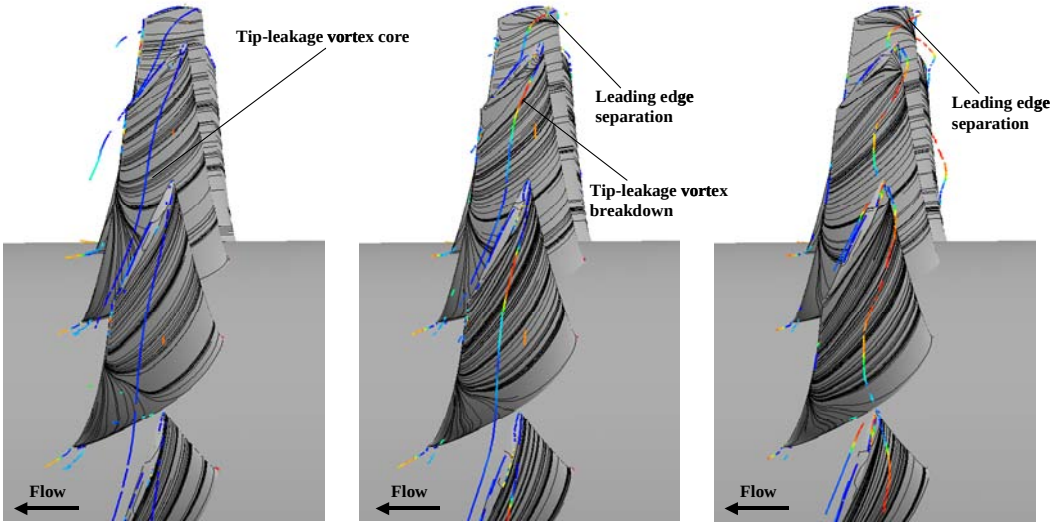

(a) Operating point A' **(b) Operating point B'** **(c) Operating point C'**

Fig. 18 Change in limiting streamline on suction surface of rotor blade at large stagger-angle setting

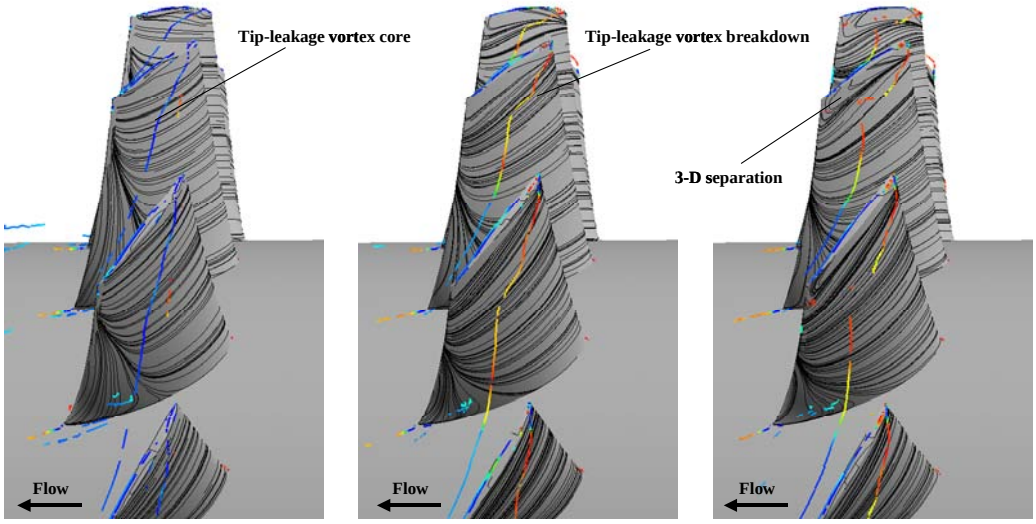

(a) Operating point D' **(b) Operating point E'** **(c) Operating point F'**

Fig. 19 Change in limiting streamline on suction surface of rotor blade at design stagger-angle setting

found that three-dimensional separation occurs at the tip and that this separation suppresses the secondary flow near the hub. The tip-leakage vortex breakdown occurs at operating points E' and F'. It is confirmed that the tip-leakage vortex breakdown induces the three-dimensional separation on the suction surface at the stall condition.

At the small stagger-angle setting shown in Fig.20, the strong outward secondary flow is observed near the trailing edge at operating points G' and H'. Moreover, three-dimensional separation occurs near the leading edge at the rotor tip at operating point G'. However, this separation does not occur at operating point H'. A focus of the separation is observed near the trailing edge on the suction surface at operating point I'. The vortex core near the trailing edge stands from the focus of the separation and reaches the leading edge of the adjacent blade. It is considered that the three-dimensional separation vortex, which stands on the suction surface near the trailing edge, develops at the operating point I'. It is also considered that three-dimensional separation vortex is induced by the tip leakage vortex breakdown.

As shown in the previous paper [12], the development of the long length-scale stall cell from the rotating instability was experimentally observed, and the occurrence of the tip-leakage vortex breakdown was numerically confirmed at the large stagger-angle setting for the moderate loaded rotor blades with hub to tip ratio of 0.57. Moreover, the development of the short length-scale stall cell was experimentally observed, and the occurrence of the tip-leakage vortex breakdown and the development of the tree-dimensional separation vortex were numerically confirmed at the design stagger-angle setting. It is found from the experimental and the numerical results of the highly and moderate loaded rotors that the development of the three-dimensional separation vortex induced by the tip-leakage vortex breakdown influences the initiation of the short length-

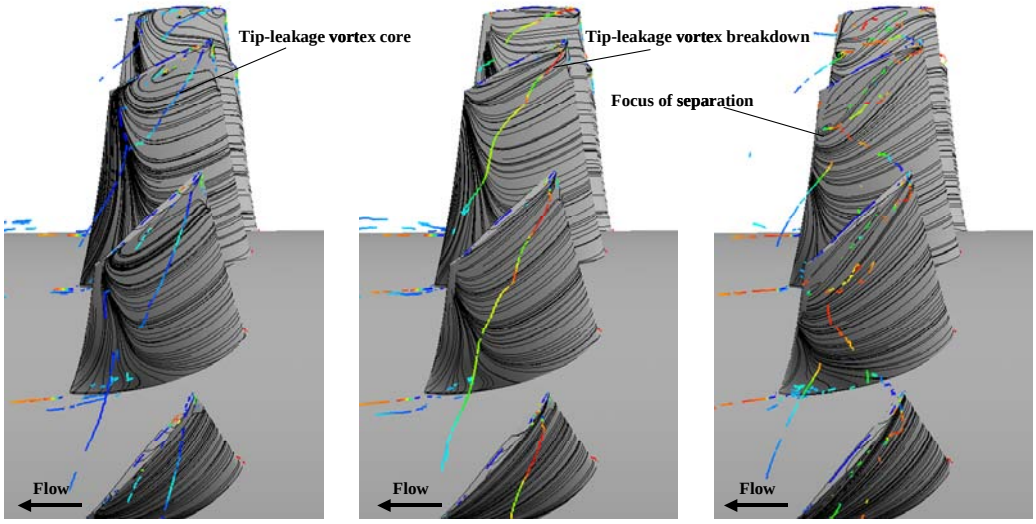

(a) Operating point G' **(b) Operating point H'** **(c) Operating point I'**

Fig. 20 Change in limiting streamline on suction surface of rotor blade at small stagger-angle setting

scale stall cell.

CONCLUSIONS

Stall inception patterns at three stagger-angle settings for the highly loaded rotor blades were experimentally investigated in a low-speed axial-flow fan. Rotor-tip flow fields were also numerically investigated to clarify the mechanism behind the stall inception from a rotating instability. Our findings of these investigations can be summarized as follows:

(1) The rotating instability is confirmed at the high stagger-angle settings for the highly loaded rotor blades as same as that for the moderate loaded rotor blades. The rotating instability is induced by an interaction between the incoming flow, the reversed tip-leakage flow, and the end-wall backflow from the trailing edge.

(2) At the high stagger-angle settings for the rotor blades, the backflow from the trailing edge initiates, and the interface between the incoming flow and the reversed tip leakage flow becomes parallel to the leading edge plane near and at the stall condition. Moreover, the tip leakage flow spills from the leading edge of the adjacent blade at the stall condition. The change in the end-wall flow at the rotor tip are consistent with the criteria for the spike initiation suggested by Vo et al. and Hah et al.. However, the short length-scale stall cell is not observed at the high stagger-angle settings.

(3) The tip-leakage vortex breakdown is confirmed at the three stagger-angle setting for the highly loaded rotor blades. The end-wall blockage induced by the tip-leakage vortex breakdown influences the development of the stall cell.

(4) The development of the three-dimensional separation vortex induced by the tip-leakage vortex breakdown seems to be one of the critera for spike-type stall inception.

REFERENCES

[1] Day, I. J., 1993, "Stall Inception in Axial Flow Compressors," ASME J. Turbomach., 115, pp. 1-9.

[2] Camp, T. R. and Day, I. J., 1998, "A Study of Spike and Modal Stall Phenomena in a Low-Speed Axial Compressor," ASME J. Turbomach., 120, pp. 393-401.

[3] Inoue, M., Kuroumaru, M., Yoshida, S., Minami, T., Yamada, K., and Furukawa, M., 2004, "Effect of Tip Clearance on Stall Evolution Process in a Low-Speed Axial Compressor Stage," ASME Paper No. GT2004-53354.

[4] Garnier, V. H., Epstein, A. H., and Greitzer, E. M., 1991, "Rotating Wave as a Stall Inception Indication in Axial Compressors," ASME J. Turbomach., 113, pp. 290-301.

[5] Mailach, R., 1999, "Experimental Investigation of Rotating Instabilities in a Low-Speed Research Compressor," IMech 1999 C557/006, pp. 595-604.

[6] Mailach, R., Lehmann, I., and Vogeler, K.,2001, "Rotating Instabilities in an Axial Compressor Originating from the Fluctuating Blade Tip Vortex," ASME J. Turbomach., 123, pp. 453-463.

[7] März, J., Gui, X., and Neise, W.,1999, "On the Structure of Rotating Instabilities in Axial Flow Machines," ISABE 99-7252.

[8] März, J., Hah, C., and Neise, W., 2002, "An Experimental and Numerical Investigation into the Mechanisms of Rotating Instability," ASME J. Turbomach., 124, pp. 367-375.

[9] Nishioka, T., Kuroda, S., and Kozu, T., 2003, "Influence of Rotor Stagger-angle on Rotating Stall Inception in an Axial-Flow Fan," ASME Paper No. GT2003-38259.

[10] Nishioka, T., Kuroda, S., Nagano, T., and Hayami, H., 2006, "Influence of Rotating Instability on Stall Inception Patterns in a Variable-Pitch Axial-Flow Fan," ASME Paper No. GT2006-90589.

[11] Nishioka, T., Kanno, T., and Hayami, H., 2007, "Characteristics of End-Wall Flow at Spike and Modal Stall Inceptions in a Variable-Pitch Axial-Flow Fan," ASME Paper No. GT2007-27738.

[12] Nishioka, T., Kanno, T., and Hayami, H., 2008, "Rotating Stall Inception from Spike and Rotating Instability in a Variable-Pitch Axial-Flow Fan," ASME Paper No. GT2008-51466.

[13] Nishioka, T., Kanno, T., and Hayami, H., 2010, "Rotor-tip flow fields near inception point of modal disturbance in an axial-flow fan," ASME Paper No. GT2010-22187.
[14] Vo, H. D., Tan, C. H., and Greitzer, E. M., 2005, "Criteria for Spike Initiated Rotating Stall", ASME Paper GT2005-68374.
[15] Hah, C., Bergner, J., and Schiffer, H. P., 2006, "Short length-Scale Rotating Stall Inception in a Transonic Axial Compressor – Criteria and Mechanisms", ASME Paper GT2006-90045-68374.
[16] Furukawa, M., Inoue, M., Saiki, K., and Yamada, K., 1999, "The role of Tip Leakage Vortex Breakdown in Compressor Rotor Aerodynamics," ASME J. Turbomach., 121, pp. 469-480.
[17] Furukawa, M., Saiki, K., Yamada, K., and Inoue, M., 2000, "Unsteady Flow Behavior Due to Breakdown of Tip Leakage Vortex in an Axial Compressor Rotor at Near-Stall Condition," ASME Paper No. 2000-GT-0666.